Influence of Trace Amount of Well-Dispersed Carbon Nanotubes on Structural Development and Tensile Properties of Polypropylene

10 AUTHORS, INCLUDING:

Kevin L. White
Kyushu University
31 PUBLICATIONS   **128** CITATIONS

Taiki Hoshino
RIKEN
26 PUBLICATIONS   **113** CITATIONS

Hiroshi Jinnai
Tohoku University
234 PUBLICATIONS   **4,241** CITATIONS

Atsushi Takahara
Kyushu University
487 PUBLICATIONS   **8,525** CITATIONS

Influence of Trace Amount of Well-Dispersed Carbon Nanotubes on Structural Development and Tensile Properties of Polypropylene

Peng Liu,[†,||] Kevin L. White,[†,||] Hiroaki Sugiyama,[‡] Jiang Xi,[§] Takeshi Higuchi,[§] Taiki Hoshino,[§] Ryohei Ishige,[§] Hiroshi Jinnai,[§] Atsushi Takahara,[§] and Hung-Jue Sue*[,†]

[†]Polymer Technology Center, Department of Mechanical Engineering, Texas A&M University, College Station, Texas 77843, United States

[‡]Kaneka Corporation, Takasago, Japan

[§]Institute for Materials Chemistry and Engineering, Kyushu University, Fukuoka, Japan

S *Supporting Information*

ABSTRACT: Functionalized multiwalled carbon nanotubes (F-MWCNTs) were individually dispersed in a commercial polypropylene (PP) matrix using our well-established α-zirconium phosphate (ZrP) nanoplatelet-assisted dispersion approach. The F-MWCNTs remained uniformly dispersed in PP after melt mixing and injection-molding and were found to remarkably enhance modulus and strength at only 0.1 wt % loading. The individual F-MWCNTs were mostly oriented and extended in the flow direction and were shown to be integrated within the crystalline structure of the matrix. The change in mechanical properties is attributed to both the modification in crystal structure due to MWCNT-induced nucleation and the direct reinforcement of crystalline lamellae and amorphous regions by the MWCNTs. We propose that the compatibilized F-MWCNTs exhibit sufficient interfacial interaction with the PP matrix to anchor lamellae stacks and resist interlamellar slip. The F-MWCNTs also reinforce amorphous domains between crystallites and behave as "super"-tie chains, thereby achieving improvement in tensile properties at low MWCNT loading. This approach for nanocomposite preparation is scalable and easily adapted for other thermoplastics by proper MWCNT surface functionalization.
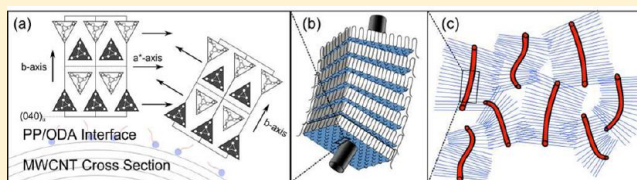
1. INTRODUCTION

Carbon nanotubes (CNTs) are a class of high aspect ratio, multifunctional nanomaterials that have been extensively investigated as filler materials to enhance the physical and mechanical properties of polymers. In order to effectively modify the performance of a polymer with low CNT loading, the individual nanofillers must be well dispersed, which increases the interfacial area between the CNTs and polymer matrix.[1] In nonpolar, commodity polymers, such as polyethylene (PE) and polypropylene (PP), compatibility is an additional concern because of the lack of interaction between the CNTs and polymer matrix.

For commercial applications, dispersion by mechanical shearing in the melt is preferable to achieve high volume production but generally fails to provide good dispersion even at optical resolution scale. Extreme shearing conditions are often required to disrupt large aggregates, but significantly reduce the length and damage the CNTs, and may degrade the polymer matrix.[2−4] Chemical surface modification may be used to improve the dispersion state and compatibility of the CNTs prior to mixing, which reduces the mechanical energy required during melt processing. However, achieving excellent dispersion usually requires extensive chemical treatment that may significantly modify the CNT properties and reduce aspect ratio.[2,4−6] These challenges are a consequence of the enormous length-dependent interaction potential between CNTs[7] and are

responsible for the current lack of fundamental knowledge and broad disagreement regarding how CNTs influence polymer properties.[8]

PE and PP make up the vast majority of worldwide polymer production because they are inexpensive, easily processable, and highly versatile. There has been substantial interest in developing PP/CNT composites with enhanced performance at sufficiently low loading to retain these advantageous properties. It is well-established that CNTs are effective α-form crystal nucleating agents for PP and significantly reduce spherulite size, enhance crystallization kinetics, and increase crystallization temperature.[3,9−12] However, there is generally no significant change in degree of crystallinity, crystal structure, or dynamic mechanical relaxation behavior.[12,19−23] Despite promising reports that have shown CNTs can significantly improve dimensional stability, reduce cycle time, decrease combustion heat release rate, and improve thermal stability,[12−18] the ability of CNTs to enhance mechanical properties of PP has been limited. To effectively utilize and identify the contribution of CNTs in reinforcing semicrystalline thermoplastics, scalable processing approaches to disentangle and

stabilize the CNTs before and after mixing in the polymer matrix are needed.

In this work, we correlate the tensile behavior of a commercial PP containing multiwalled carbon nanotubes (MWCNTs) with the microstructure of the system across broad length scales. Excellent dispersion and compatibilization were achieved using our well-established nanoplatelet-assisted dispersion approach,[24−26] followed by subsequent reaction with octadecylamine (ODA),[18] which is a long-chain fatty amine functional group well-known to be miscible with PP. This unique processing method takes advantage of the reversible electrostatic interaction between exfoliated α-zirconium phosphate (ZrP) nanoplatelets, which have a positive surface charge, and lightly oxidized CNTs. During ultrasonication, the high aspect ratio ZrP nanoplatelets focus mechanical energy within CNT aggregates and promote their individual dispersion in aqueous solvent.[24−26] The concentration of energy across the surface of the CNTs prevents significant stretching or bending of the nanotubes during sonication that would otherwise result in the rupture and scission of long CNTs.[5,6] The ZrP nanoplatelets may be subsequently removed from solution by the introduction of an acid to disrupt the electrostatic interaction between the ZrP and CNT phases.[25,26] We have recently reported that this method results in high yield (>95%) of individually dispersed single-walled carbon nanotubes (SWCNTs) and MWCNTs in aqueous solution, while completely removing any detectable trace of the ZrP nanoplatelets.[24,26]

In our previous work, we showed that after reacting with ODA, the recovered functionalized MWCNTs (F-MWCNTs) are stable in PP and remain well dispersed at up to 2 wt % loading in compression-molded samples.[18] The disentanglement process is extremely beneficial for properties related to the surface area of the F-MWCNTs, such as thermo-oxidative stability, the onset of electrically conductive behavior, and PP crystallite nucleation. In this work, we report remarkable improvements in the mechanical properties of injection-molded PP containing only 0.1 wt % F-MWCNTs. The structure of the PP/F-MWCNT nanocomposites is investigated across several length scales in order to elucidate the microstructural mechanisms responsible for the observed behavior. The implications of the present findings for engineering applications of nanoparticle-filled polymers are discussed.

2. EXPERIMENTAL SECTION

2.1. Materials. Pristine MWCNTs (P-MWCNTs) (purity >90%, average outer diameter of 10−12 nm, and length of 0.1−10 μm) and ODA ($CH_3(CH_2)_{17}NH_2$, 97%) were purchased from Sigma-Aldrich. The P-MWCNTs were purified by mild oxidation and disentangled with exfoliated ZrP nanoplatelets using our established nanoplatelet-assisted dispersion approach.[24−26] The ZrP nanoplatelets were synthesized with length and width of 100 μm and exfoliated to an individual layer thickness of 0.7 nm using tetra(n-butylammonium hydroxide) (Sigma-Aldrich, 1 mol L^{-1} in methanol), which has been previously reported in detail.[27−29] The disentangled MWCNTs were isolated from solution by the addition of acid to coagulate and precipitate the ZrP nanoplatelets.[25,26] The disentangled MWCNTs were functionalized with ODA prior to mixing with PP according to our recently reported method.[18] The MWCNTs become hydrophobic after reacting with ODA and precipitate from aqueous solution. The recovered F-MWCNTs were thoroughly washed and dried in an oven overnight at 80 °C.

2.2. Preparation of PP/MWCNT Composites. The F-MWCNTs were added to xylene and sonicated for 1 h at room temperature. PP pellets were added to the F-MWCNT/xylene solution and stirred for 1

h at 125 °C to obtain a masterbatch with 2 wt % F-MWCNT. Ethanol was added to precipitate the PP/F-MWCNT from solution. The recovered powder was washed several times and dried under vacuum overnight at 80 °C. The PP/F-MWCNT masterbatch was compounded with PP to concentrations of 0.1 and 0.6 wt % using a System 40 Haake mixer at 60 rpm and 180 °C for 2 min. For comparison, PP/P-MWCNT (0.1 wt %) and PP/ODA (0.5 wt %) systems were prepared using the same processing conditions. Specimens were manufactured with a CS-183 MMX mini injection molder at fixed melt and mold temperatures of 195 and 90 °C, respectively, with injection rate of 0.25 cm^3/s. The molded samples were slowly cooled to room temperature.

2.3. Characterization. Samples for transmission electron microscopy (TEM) and transmission electron microtomography (TEMT) were prepared using a diamond knife to face-off trimmed block specimens from the core region prior to staining. The faced-off block was exposed to vapor from an aqueous solution containing 0.5 wt % RuO_4 for 12 h. Ultrathin sections were prepared using a Reichert-Jung Ultracut E microtome with diamond knife at cryogenic temperature. TEM specimens were prepared with thickness of 60−80 nm. Thin sections were placed on a 300-mesh Formvar-coated copper grid and examined using a JEOL 1200 EX TEM operating at an accelerating voltage of 100 kV. For TEMT, thin sections of PP/F-MWCNT (0.1 wt %) were prepared with thickness of about 150 nm. A JEOL JEM-2200FS computerized TEM operating at an accelerating voltage of 200 kV was used to record a series of 135 projections along a single tilt axis at tilt angles ranging from −67° to 66° with an angular interval of 1°. The images were aligned using Au colloidal beads deposited on the thin section surface. The positions of 14 Au nanoparticles were tracked throughout the series of tilted images.[30,31] The images were acquired at resolution of 0.36 nm/pixel. The maximum calculated deviation between the aligned images was ±0.8 pixel.

Optical microscopy (OM) specimens of injection-molded PP nanocomposites with dimensions of 5 × 5 × 2.5 mm^3 were cut from the core region and polished. The specimens were etched with an oxidizing solution containing 3 wt % potassium permanganate in mixed solvent of sulfuric acid and phosphoric acid to preferentially attack the amorphous regions of the polymer.[29] Specimens were examined using an Olympus BX60 OM under bright-field conditions in reflectance mode.

X-ray diffraction specimens were cut from the core region of injection-molded samples with dimensions of 5 × 5 × 2.5 mm^3. The incident X-ray beam was perpendicular to the molding direction for both wide-angle X-ray diffraction (WAXD) and small-angle X-ray scattering (SAXS) measurements. WAXD experiments were performed with a Bruker-AXS D8 diffractometer with Cu Kα radiation (wavelength, λ = 0.154 nm) operating at 40 kV and 50 mA. Specimens were placed inside an aluminum sample holder and scanned at room temperature over diffraction angle, 2θ, from 2° to 70° with step size of 0.03°. The WAXD results were normalized relative to the total scattering intensity of each specimen. SAXS measurements were performed at room temperature using a synchrotron X-ray radiation source (BL40-B2 beamline, λ = 0.1 nm) at the SPring-8 synchrotron research facility in Hyogo Prefecture, Japan. Scattered X-rays were detected using a 3000 × 3000 pixel imaging plate over a scattering vector range of 0.05 nm^{-1} < q < 4 nm^{-1}. The scattering vector, q = $4\pi(\sin\theta)/\lambda$, was calibrated based on the average of three peaks of silver behenate with a sample-to-detector distance of 2.2 m. All SAXS measurements were corrected for intensity fluctuations in the main beam and sample absorption. The scattering intensity was corrected to account for background scattering.

Dynamic mechanical behavior was investigated using an ARES-G2 rheometer (TA Instruments) in torsional mode. The strain amplitude was 0.01%, which was verified to be within the linear viscoelastic region of all samples at −20 °C. The temperature was ramped at a constant rate of 3 °C/min from −20 to 150 °C at fixed frequency of 1 Hz. The glass transition temperature, T_g, was assigned to the temperature associated with the first maximum in tan δ = G''/G', where G'' and G' are the loss and storage moduli, respectively.
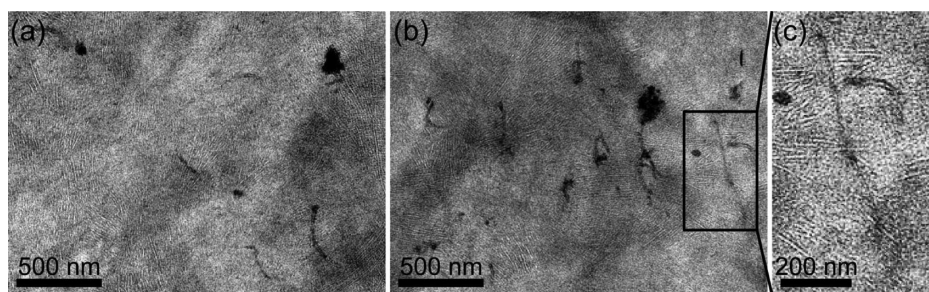
Figure 1. TEM images of stained PP/F-MWCNT nanocomposites demonstrating homogeneous dispersion of the MWCNTs: (a) PP/F-MWCNT (0.1 wt %); (b) PP/F-MWCNT (0.6 wt %); (c) higher magnification of (b) showing detail of lamellae structure and oriented F-MWCNT. Flow direction is from bottom to the top of the images.
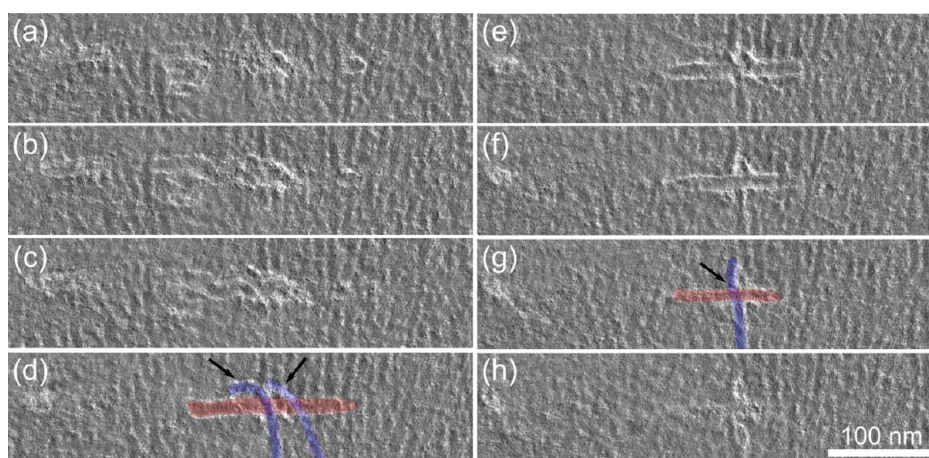

Figure 2. Sequence of TEMT slices of PP/F-MWCNT (0.1 wt %) nanocomposite obtained from serial tilt projections. Each image represents a 0.36 nm slice through the thickness of the sample. Sequential images are separated by 3.6 nm along the z-axis. A single horizontally oriented MWCNT is centered in each image. The PP lamellae are oriented perpendicular to the long axis of the F-MWCNT are aligned vertically.

Tensile tests were carried out in accordance with ASTM D638-08. Room temperature tensile tests were performed on an MTS screw-driven test machine with crosshead speed of 5 mm/min. True strain was measured using a calibrated MTS contact extensometer, model 632 12B-50, and was verified with a MTS LX1500 laser extensometer. The initial gauge length of the tensile specimens was 25.4 mm. The reported standard deviation in elastic modulus, E, and tensile yield strength, σ_y, are based on at least five specimens.

3. RESULTS

3.1. Dispersion and Microstructure. The dispersion of F-MWCNTs and crystalline morphology of PP in the injection-molded composites were investigated with TEM. The micrographs clearly show that the disentangled F-MWCNTs remain individually dispersed after molding (Figure 1). At 0.1 wt % loading, the injection-molded F-MWCNTs appear to be highly extended and oriented in the molding direction. The microstructure of the PP/F-MWCNT (0.6 wt %) consists of much closer spaced MWCNTs that are similarly extended and preferentially oriented in the flow direction. In our previous report on compression-molded samples, the uniformly dispersed F-MWCNTs are randomly oriented and partially coiled in the PP matrix.[18] This suggests that the shearing forces during molding conditions are responsible for the orientation and conformation of the F-MWCNTs. Although it is difficult to precisely determine the dispersion using TEM, the dispersion quality of the 0.6 wt % F-MWCNT system appears to be reduced compared to the dispersion at lower loading. The spherical, black inclusions in the image are attributed to

catalyst-induced phase-separated domains of the ruthenium heavy metal from the staining solution. Elemental analysis confirmed the presence of iron and ruthenium heavy metal species in the spherical aggregates.

After extensive TEM analysis, we concluded that in the vicinity of the F-MWCNTs, the PP lamellae are predominantly oriented perpendicular to the F-MWCNT axis (Figure 1c). The highly ordered interface extends along the entire F-MWCNT length, which is consistent with previous reports on CNT-induced transcrystallinity in PP.[22,33,34] The total diameter of the transcrystalline regions appears to be relatively small and localized near the CNTs. It is important to note that conventional 2D TEM provides only limited information regarding the PP/CNT interface because the spatial association among the observed structural features is not clear. The influence of the F-MWCNTs on the 3D morphology of the PP matrix was elucidated with TEMT. A series of micrographs were obtained over a broad range of tilting angles and were subsequently aligned using Au nanoparticles deposited on the surface. This technique has previously been applied to study the complex morphology of various systems including block copolymers[35−38] and polymer nanocomposites,[39−42] although we are unaware of any previous TEMT investigations on a CNT-filled polymer. The calculated error in image alignment is less than the resolution of the images.

A series of TEMT slices through the thickness of the PP/F-MWCNT (0.1 wt %) sample are shown in Figure 2. The images are centered on a single horizontally oriented F-MWCNT, and the PP crystalline lamella appear vertically

oriented. The image progression corresponds to an incremental slicing through the thickness of the TEMT specimen (z-axis). The individual images represent 0.36 nm thick projections, and each sequential image in Figure 2 is separated by 3.6 nm along the z-axis. The observed PP lamellae are therefore positioned less than 0.36 nm from the F-MWCNTs, which verifies that the features are spatially associated. The F-MWCNT and well-defined PP lamellae in Figures 2d and 2g are lightly shaded to improve clarity. An accompanying high-resolution TEMT video showing the detailed microstructure and interaction between the F-MWCNT and PP lamellae at lower magnification is provided in the Supporting Information.

The F-MWCNT shown in Figure 2 is about 500 nm long but appears shorter because of the narrow depth of field for the individual images. The position of the F-MWCNT also appears to shift throughout the image series due to its waviness in the z-direction. The position of the lamellae shifts with the F-MWCNTs, which indicates that the orientation of the PP lamellae follows the curvature of the nanotubes at the interface and confirms that the lamellae extend radially from the F-MWCNT surface as extended, 2D stacks. In Figure 2d, two black arrows highlight a pair of PP lamellae, shaded blue, that are clearly positioned above the surface of the F-MWCNT, which is shaded red. The image in Figure 2g is 10.8 nm below the image in Figure 2d along the thickness direction and shows one of the indicated lamellae clearly positioned beneath the F-MWCNT. These images conclusively demonstrate that the F-MWCNT is intermingled with the crystalline lamellae as well as the amorphous layers that interconnect the lamellae stacks. Further work is being pursued to generate volume-rendered 3D images to better elucidate the global morphological features of this system.

The bulk crystal structure of the PP nanocomposites was investigated using OM and is shown in Figure 3. The neat PP exhibits a characteristic spherulitic structure with clearly defined boundaries and average diameter on the order of 30 μm (Figure 3a). In the PP/F-MWCNT (0.1 wt %) (Figure 3b) and PP/F-MWCNT (0.6 wt %) (Figure 3c) systems, the individual spherulites are no longer clearly visible, which is attributed to extensive heterogeneous nucleation of PP crystallites from the
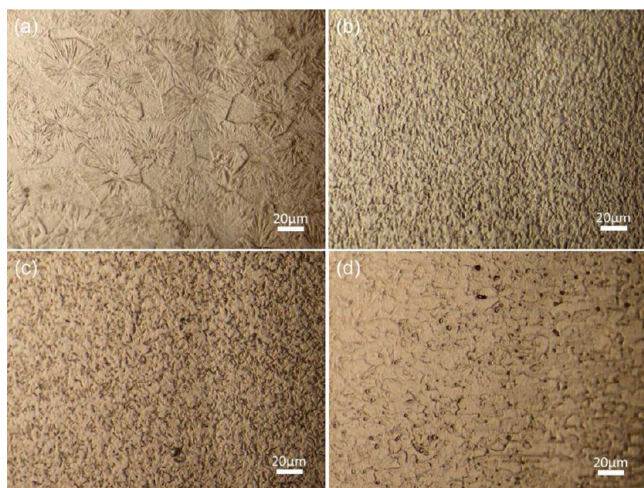
well-dispersed F-MWCNTs. Both systems exhibit highly uniform microstructure and show no evidence of macroscopic clustering or aggregation. In contrast, the crystalline morphology of the PP/P-MWCNT system (Figure 3d) consists of visible MWCNT agglomerates that appear to be preferentially localized at grain boundaries between spherulites. Specimens containing 0.5 wt % ODA exhibit spherulitic morphology similar to the neat PP, with spherulite diameter increased to 50−60 μm (Supporting Information Figure 1). This behavior is characteristic of a miscible functional group, which we previously observed from differential scanning calorimetry (DSC) measurements of compression-molded samples.[18]

3.2. Crystal Structure. The WAXD patterns are shown in Figure 4, and several relevant structural parameters are
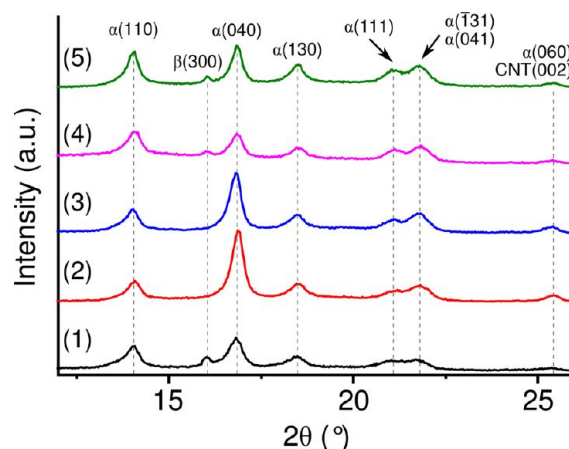

Figure 4. WAXD patterns of injection-molded PP composite materials: (1) neat PP, (2) PP/F-MWCNT (0.1 wt %), (3) PP/F-MWCNT (0.5 wt %), (4) PP/P-MWCNT (0.1 wt %), and (5) PP/ODA (0.5 wt %).

Table 1. Summary of Crystal Structure Parameters from WAXD Investigation for Injection-Molded PP Nanocomposites[a]

	K (%)	$I_{(110)}/I_{(040)}$	fwhm (deg)	
			(110)	(040)
neat PP	14.6 ± 2.3	0.87	0.56 ± 0.02	0.56 ± 0.02
0.1 wt % F-MWCNT	0	0.33	0.38 ± 0.01	0.36 ± 0.02
0.6 wt % F-MWCNT	0	0.43	0.42 ± 0.01	0.36 ± 0.01
0.1 wt % P-MWCNT	15.3 ± 0.5	1.03	0.52 ± 0.02	0.53 ± 0.02
0.5 wt % ODA	11.5 ± 1.9	1.15	0.51 ± 0.02	0.44 ± 0.02

[a]K is empirical factor describing percentage of β-form crystals contained within the total crystal content of the PP matrix, calculated from eq 1; $I(110)/I_{(040)}$ is ratio of relative intensity of reflections on (110) and (040) lattice planes; fwhm is the full width at half-maximum for reflection on specified planes.

Figure 3. Optical micrograph of PP composites taken from the core region of injection-molded specimens after permanganic acid etching: (a) neat PP, (b) PP/F-MWCNT (0.1 wt %), (c) PP/F-MWCNT (0.6 wt %), and (d) PP/P-MWCNT (0.1 wt %).

summarized in Table 1. Isotactic PP is polymorphic and may crystallize into monoclinic α-form, trigonal β-form, or orthorhombic γ-form crystallites, depending on processing conditions, isotacticity, and the presence of nucleating agents.[43−48] The monoclinic α-form crystal is most common and is responsible for the diffraction peaks measured at 14.1°,
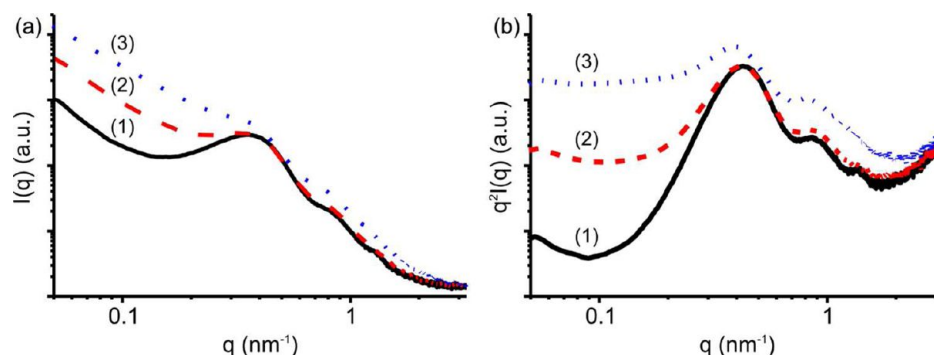
Figure 5. SAXS profiles of (1) neat PP, (2) PP/F-MWCNT (0.1 wt %), and (3) PP/F-MWCNT (0.6 wt %) systems. (a) Intensity, $I(q)$, versus scattering vector, q, and (b) Lorentz-corrected intensity, $q^2 I(q)$, versus q.

16.9°, 18.5°, and 21.2°, which are indexed to reflections on the (110), (040), (130), and (111) lattice planes, respectively. The diffraction peak at 21.8° is attributed to α-form crystal reflections on the (−131) and (041) lattice planes.[43,48] The diffraction peak at 25.5° is due to reflections on both the (060) lattice plane of the α-form crystal and the (002) graphitic plane of the MWCNTs.[49] The diffraction peak at 16.1° is due to reflections on the (300) lattice plane of the β-form crystal.[50] Diffraction associated with the γ-form crystal is typically observed as sharp peaks near 15.0° and 20.2°, which were not observed in this work. The positions of the diffraction peaks for all injection-molded samples varied by less than the step size of the WAXD experiment and are consistent with the well-established reciprocal spacing of lattice planes in isotactic PP.[43] This indicates that there is no conformational disorder or change in d-spacing of the PP crystal unit cell due to the presence of the MWCNT or ODA.

The relative amount of β-form crystals within the total crystal content of the PP was estimated by the semiquantitative factor K introduced by Turner-Jones et al.[43] The value is a ratio of the integral intensities of crystalline reflections associated with the α-form and β-form crystal phases and is given by the expression

$$K = I_\beta / (I_{\alpha 1} + I_{\alpha 2} + I_{\alpha 3}) \tag{1}$$

where I_β is the intensity of the (300) reflection of the β-form crystal and $I_{\alpha 1}$, $I_{\alpha 2}$, and $I_{\alpha 3}$ are the intensities of the (110), (040), and (130) reflections of the α-form crystal, respectively. The neat PP in this work contains 14.6 ± 2.3% β-form crystallites, estimated from eq 1. In systems containing 0.1 and 0.6 wt % F-MWCNTs, there is a complete absence of β-form crystals, which confirms the well-known α-crystal nucleating effect of CNTs in PP.[19,20] The PP/P-MWCNT (0.1 wt %) and PP/ODA (0.5 wt %) systems do not show a significant change in K relative to the neat PP. In the PP/P-MWCNT system, the residual β-form crystal fraction is attributed to the decreased surface area of the poorly dispersed P-MWCNTs compared to the F-MWCNTs at the same loading, which limits the extent of heterogeneous nucleation. This indicates that if good dispersion can be achieved without decreasing aspect ratio, less than 0.1 wt % MWCNT is sufficient to modify the global crystal structure of PP.

The relative size, distribution, and orientation of PP crystallites were inferred from the height and breadth of reflections on the (110) and (040) planes, which are the primary reflections of α-form PP.[51] Both PP/F-MWCNT systems show a substantial increase in (040) intensity, $I_{(040)}$, and a negligible change in (110) intensity, $I_{(110)}$, compared to the neat PP, and show a significant decrease in diffraction width on both lattice planes. The decrease in $I_{(110)}/I_{(040)}$ indicates that at 0.1 wt % F-MWCNT loading there is preferential crystal growth normal to the (040) lattice plane or, equivalently, growth normal to the (110) plane is restricted.[52,53] The decrease in diffraction width suggests that the crystallite size and perfection along both primary lattice planes is increased. At higher loading of 0.6 wt % F-MWCNT, there is no further change in crystallite structure, although the slight increase in $I_{(110)}/I_{(040)}$ and diffraction width on the (110) plane may indicate a decrease in dispersion quality.

The PP/P-MWCNT (0.1 wt %) system exhibits essentially identical diffraction intensity and peak width on both primary lattice planes as the neat PP. In the PP/ODA (0.5 wt %) system, the intensities of both primary reflections are increased, and the diffraction width on the (040) lattice plane is decreases slightly, which suggests some increase crystal perfection and size. The increase in $I_{(110)}/I_{(040)}$ indicates that the presence of ODA favors crystal growth along the a^*-axis,[51] which shows that the ODA functional group is not responsible for the observed change in crystal structure in the PP/F-MWCNT systems. WAXD profiles of compression-molded systems were also obtained but revealed no significant change in crystal structure between the systems (Supporting Information Figure 2). The observed differences in WAXD patterns for the injection-molded samples are therefore attributed to the alignment and extension of the MWCNTs during molding and the corresponding change in PP crystal orientation and growth behavior.

The diffraction intensity at 25.5°, normalized relative to the dominant (110) reflection of the PP matrix, is not significantly affected by the introduction of 0.1 wt % P-MWCNT or 0.5 wt % ODA but increases by a factor of 3.2 and 3.8 in PP composites containing 0.1 and 0.6 wt % F-MWCNT, respectively. This is significantly greater than the observed increase in $I_{(040)}$, which suggests that the increased intensity at 25.5° is primarily due to the (002) graphite reflection of F-MWCNTs aligned in the molding direction. At 0.6 wt % F-MWCNT loading, although $I_{(110)}/I_{(040)}$ decreases, the relative intensity of the diffraction peak at 25.5° increases, which is consistent with an increased number of (002) graphitic lattice planes due to MWCNTs aligned in the molding direction.

OM and WAXD investigations revealed that the long-range and atomic-scale features of the PP crystal microstructure, respectively, are significantly modified by the addition of F-MWCNTs. SAXS is sensitive to the intermediate-range repeat unit structure of PP and was measured through the thickness of

the injection-molded samples using synchrotron radiation. The 2D SAXS pattern of the neat PP shows isotropic scattering characteristic of a population of spherically symmetric assemblies containing stacked lamellar structure with regular crystalline−amorphous microstructure (Supporting Information Figure 3). Both PP/F-MWCNT systems exhibit similar symmetry, which indicates that the preferential crystallite orientation observed with WAXD does not result in anisotropy over longer length scales.

The azimuthally averaged SAXS patterns are shown in Figure 5. The first maxima, q_1, is related to the alternating crystalline−amorphous microstructure of the PP lamellae and can be used to calculate the long period, L, using Bragg's law, where $L = 2\pi/q_1$. The long period is the average sum of the crystalline lamellae thickness and the thickness of amorphous regions between crystallites and was determined from the Lorentz-corrected intensity profile to account for the random distribution of lamellae orientations in reciprocal space. The long period of the neat PP is $L^{LC} = 15.47$ nm. The addition of 0.1 wt % F-MWCNT causes a negligible change in L^{LC}, and at higher loading of 0.6 wt % F-MWCNT, L^{LC} increases to 16.72 nm. Increasing long period with CNT loading has been previously reported and attributed to an increase in lamellae thickness.[54] However, we were unable to find sufficient TEM evidence to support this claim and observed no change in degree of crystallinity from either WAXD or DSC measurements to suggest a change in crystalline fraction (not shown). It is more likely that the increase in long period is due to scattering from the MWCNT phase. The MWCNTs used in this work have inner diameter of ∼5−6 nm, which should increase scattering intensity for $q < 1/R = 0.3−0.4$ nm^{-1}. This is in excellent agreement with results for the PP/F-MWCNT (0.1 wt %) system, which show no significant deviation in intensity from the neat PP until about 0.35 nm^{-1}. The scattering intensity of the PP/F-MWCNT (0.6 wt %) is increased over all values of q, which is attributed to scattering between more closely spaced F-MWCNTs.

For the neat PP, additional scattering maxima are clearly defined at higher q and show a nearly integer relationship with q_1: $q_2/q_1 = 1.96$ and $q_3/q_1 = 3.10$. This integer ratio between maxima is characteristic of a periodic lamellae microdomain structure.[55] The ratio between q_2 and q_1 is not affected by F-MWCNT loading: $q_2/q_1 = 2.00$ and 2.01 for the PP/F-MWCNT (0.1 wt %) and PP/F-MWCNT (0.6 wt %) systems, respectively. The third maxima, q_3, does not change with 0.1 wt % F-MWCNT loading but could not be discerned at 0.6 wt % F-MWCNT loading, which is attributed to the increased background scattering at high q. On the basis of the SAXS measurements, it is apparent that the F-MWCNTs do not significantly modify the intermediate-range microdomain structure of the PP matrix.

The 3D microstructure of the isotropic composite systems was further probed using the 1D correlation function, γ_1 (Supporting Information Figure 4). Details on the calculation can be found in our previous work on SAXS of oriented poly(ethylene terephthalate).[56] The long period, L^{SC}, was calculated from the second maxima in the correlation curve based on the self-correlation triangle method described by Strobl and Schneider.[57] The intercept of the initial portion of the correlation curve and the horizontal tangent of the first minima provide an estimate of the thickness of one phase, L_1. Assuming a simple two-phase model with sharp interfaces between crystalline and amorphous domains, the thickness of

the second phase may be calculated from the expression $L_2 = L^{SC} − L_1$ and was found to slightly increase with F-MWCNT loading. Based on TEM evidence, L_2 is the lamellae thickness, which indicates that L_1 is the thickness of amorphous regions between lamellae. A summary of the lamellae and interlamellar thicknesses determined from SAXS measurements is provided in Table 2. The 1D correlation function shows a significant

Table 2. Summary of SAXS Measurements of Injection-Molded PP Composites[a]

	L^{LC} [nm]	L^{SC} [nm]	L_1 [nm]	L_2 [nm]
neat PP	15.47	14.82	3.1	11.7
0.1 wt % F-MWCNT	15.51	14.85	3.0	11.9
0.6 wt % F-MWCNT	16.72	15.75	2.7	13.1

[a]L^{LC} is long period determined from Lorentz-corrected SAXS profile; L^{SC} is long period determined from second maxima in the 1D correlation function, γ_1; L_1 is the thickness of amorphous domains between lamellae; L_2 is the lamellar thickness.

decrease in the depth of the primary minimum and height of the maximum with increasing F-MWCNT content. This may indicate diminished packing efficiency in the crystalline regions at 0.6 wt % F-MWCNT loading, which also decreases interlamellar spacing, L_1, to maintain constant degree of crystallinity. At 0.1 wt % F-MWCNT loading, there is no significant change in thickness measurements from the neat PP, which supports our claim that the F-MWCNTs are extremely well integrated with the lamellar structure. However, due to the similarity in dimensions of the PP lamellae thickness and the MWCNT diameter, further work is necessary to substantiate this interpretation.

3.3. Dynamic Mechanical Analysis. The DMA curves of the injection-molded PP composites are shown in Figure 6. For clarity, only the neat PP and PP/F-MWCNT systems are shown. The remaining systems are provided in Supporting Information Figure 5. The storage modulus of the neat PP exhibits a relatively narrow plateau region approaching $T_g = 6.6$ °C, followed by a progressive decrease with temperature due to cooperative relaxation within amorphous domains. The loss factor, tan δ, is a measure of the damping ability of a material and provides a sensitive measure of molecular-scale motion and relaxation in semicrystalline polymers. Slightly above the low-temperature maxima in tan δ corresponding to T_g, there is a broad mechanical relaxation extending from 55 to 125 °C, with peak at $T_\alpha = 91.6$ °C. The higher temperature α-relaxation peak of isotactic PP is generally attributed to damping within the crystalline lamellae.[50,58] Approaching 150 °C, the rapid decrease in storage modulus and corresponding increase in mechanical damping are due to the onset of crystalline melting.

The PP/F-MWCNT (0.1 wt %) system exhibits the highest storage modulus throughout the observed temperature range and shows maximum reinforcing efficiency relative to the neat PP at 95 °C, where G' is increased by about 30%. Increasing F-MWCNT loading to 0.6 wt % does not further improve storage modulus below T_g and decreases G' throughout the broad α-relaxation transition at higher temperatures. The storage modulus of PP is not significantly changed with the addition of either 0.1 wt % P-MWCNT or 0.5 wt % ODA.

Both PP/F-MWCNT systems exhibit a slight decrease in T_g, which is consistent with measurements on decreasing β-crystal content reported by Jacoby et al.[50] and Crissman.[59] The onset of the higher temperature crystalline relaxation does not vary
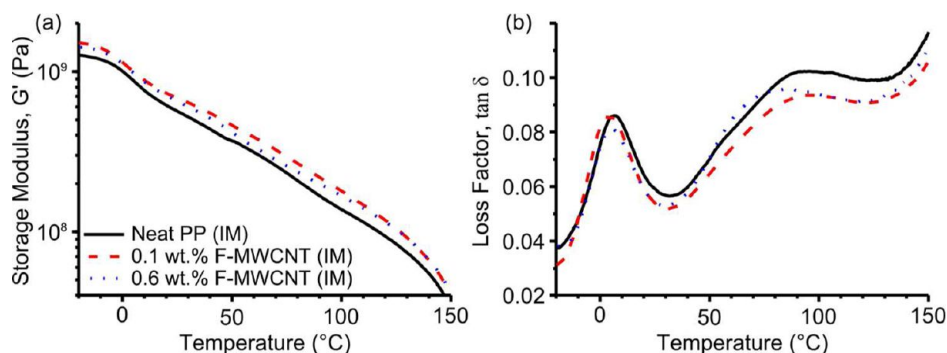
Figure 6. DMA measurements of injection-molded PP composite systems. (a) Storage modulus and (b) loss factor, tan δ, obtained from isochronal measurements at frequency of 1 Hz and ramp rate of 3 °C/min in torsion.
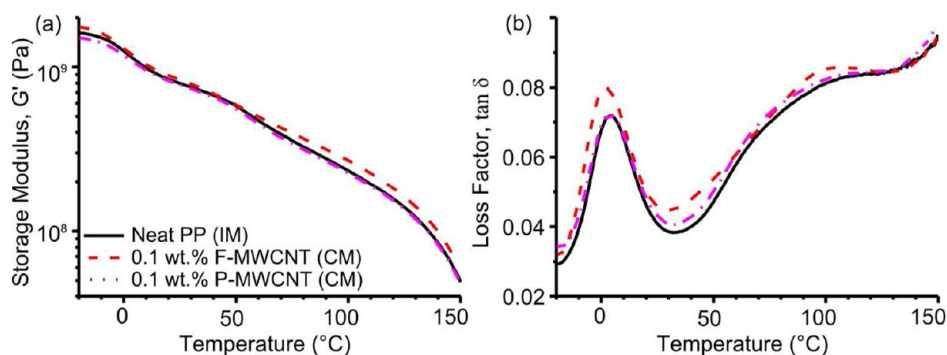

Figure 7. DMA measurements of compression-molded PP composite systems. (a) Storage modulus and (b) loss factor, obtained from isochronal measurements at frequency of 1 Hz and ramp rate of 3 °C/min in torsion.

significantly between the different systems, although the slope of tan δ is significantly increased in the PP containing F-MWCNT (0.6 wt %) and P-MWCNT (0.1 wt %). This is attributed to a greater concentration of defects and disorder within the crystalline structure. For the PP/F-MWCNT (0.1 wt %) system, the peak temperature of the α-relaxation is slightly increased and the peak intensity is decreased, which is anticipated for higher α-crystal content.[49] However, the decreased slope of tan δ is unique and cannot be attributed to the observed change in crystal structure. The decrease in temperature-dependent relaxation approaching the α-transition suggests that the F-MWCNTs are able to resist relaxation of PP chains within crystalline domains and likely also at crystalline–amorphous interfaces.

Approaching T_{α}, the amorphous domains become fully relaxed as the crystalline lamellae approaches the melt state. It is interesting to note that in this region the tan δ profiles for both PP/F-MWCNT systems are nearly identical and their respective values of G' begin to converge. At ∼130 °C and up to the onset of melting, the storage moduli of the injection-molded PP/F-MWCNT systems are identical. This suggests that the observed differences between the systems containing F-MWCNTs primarily originate from features in the amorphous region and crystalline–amorphous interfaces, which indicates that the higher loading of F-MWCNTs are not well integrated within the crystalline structure and therefore fail to provide any additional reinforcement benefit.

Clear interpretation of the molecular scale mechanisms present in the injection-molded samples is challenging because of the polymorphic character of the PP matrix and potentially frozen-in molecular orientation at the PP/F-MWCNT interface. Compression-molded samples were prepared to more

clearly elucidate interaction between the phases in the absence of multiple crystal phases, molecular orientation, or external forces (Figure 7). The T_{g} is negligibly affected by the presence of the F-MWCNTs, which indicates that the overall dynamic mechanical behavior is not significantly altered. The peak intensity of tan δ at T_{g} is significantly increased in the PP/F-MWCNT (0.1 wt %) system, and the slope of tan δ is decreased for $T > T_{g}$ (Figure 7b). Three separate samples were measured to confirm that these behaviors were consistent. The increased damping at T_{g} is not likely related to any MWCNT-induced change in the PP matrix, and there is no clear reason why the MWCNTs would directly enhance mechanical damping. The enhanced damping is therefore attributed to the presence of a fluid-like PP/ODA interface at the F-MWCNT surface, which was suggested in our previous work.[18] The compression-molded PP/ODA (0.5 wt %) system exhibits a significant decrease in G' and increase in tan δ throughout the entire temperature range, which supports this conclusion (Supporting Information Figure 5). Below T_{g}, the storage modulus is slightly increased with the addition of 0.1 wt % F-MWCNT (∼10%) and increases relative to the neat PP with temperature. No significant change in DMA spectra was observed in the PP/P-MWCNT (0.1 wt %) system relative to the neat PP.

3.4. Tensile Properties. Representative engineering stress–true strain tensile curves of the PP nanocomposites are shown in Figure 8. A summary of the tensile properties is provided in Table 3. The addition of only 0.1 wt % F-MWCNT increases elastic modulus ∼40% compared to the neat PP. To quantitatively compare the change in modulus with other works, we calculated the rate of modulus increased with respect to filler volume, dE/dV_{f}, which is a figure of merit proposed by
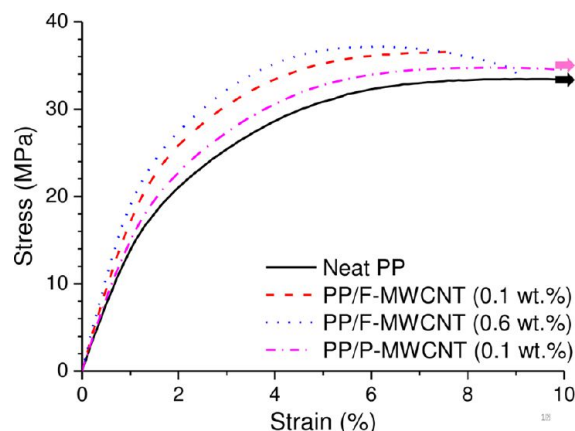
Figure 8. Tensile stress−strain curves for neat PP and nanocomposite systems.

Cadek et al.[1] Assuming that the PP matrix and MWCNTs have densities of 0.91 and 2.15 g/cm^3, respectively, $dE/dV_f \approx 1440$ GPa at 0.1 wt % F-MWCNT, which is among the largest values reported for CNT-filled polymers available in the literature.[60] We note that similar gains in mechanical properties have been privately reported to us by industry, which suggests that the improvement may be characteristic of any system containing well-dispersed, individual MWCNTs that exhibit adequate compatibility with the host polymer matrix.[61] However, we are unaware of any similar findings in the published literature. Increasing the concentration of F-MWCNTs does not further enhance modulus, and substantially diminishes the reinforcing efficiency, $dE/dV_f \approx 280$ GPa at 0.6 wt % F-MWCNT. The PP/P-MWCNT (0.1 wt %) system shows an insignificant improvement in modulus (7% increase) and relatively low reinforcing efficiency of $dE/dV_f \approx 230$ GPa. At 0.5 wt % ODA loading, the elastic modulus is decreased slightly, which further confirms that the functionalizing agent has little direct contribution to tensile behavior.

The yield strength of PP is also significantly improved due to the presence of 0.1 wt % F-MWCNT (∼16% increase), although the elongation at break is substantially decreased. Analysis of the tensile fracture surface revealed that fracture occurs following neck formation and limited drawing in the tensile direction. Significant stress whitening was also observed, which indicates that the PP lamellae exhibit limited plastic deformation prior to fracture. In the PP/F-MWCNT (0.6 wt %) system, fracture occurs without any evidence of yielding, necking behavior, or stress whitening. The tensile fracture surface was smooth and characteristic of brittle fracture in a glassy polymer. The incorporation of 0.1 wt % P-MWCNT does not significantly influence any of the tensile properties of the PP matrix, which we attribute to poor dispersion and a lack

of interaction between phases. The yield strength of the PP/ODA (0.5 wt %) system is increased slightly (∼10%), and ductile fracture was observed with a moderate decrease in elongation at break. The decrease in ε_B for PP/ODA is likely due to the increase in spherulite radius, which typically causes failure at weak interspherulitic boundaries due to the formation of voids during thermal contraction, and segregation of impurities.

Compression-molded samples were prepared to investigate whether the observed changes in mechanical properties may be due to processing conditions or crystal structure (Table 3). The unfilled compression-molded PP exhibits a slightly higher modulus, no change in yield strength, and lower elongation at break than the injection-molded PP. These results are in agreement with previous reports on the influence of β-form crystal fraction on mechanical properties.[62] The compression-molded PP/F-MWCNT (0.1 wt %) shows a much smaller increase in modulus relative to the injection-molded sample and negligible change in σ_y compared to the neat PP. This indicates that the improvement in elastic modulus must be partially attributed to the α-nucleating ability of the MWCNTs but does not account for the increase in yield strength. The mechanical properties of the compression-molded PP/P-MWCNT (0.1 wt %) are nearly identical to the neat PP, which further supports that there is no significant interaction between the phases.

4. DISCUSSION

The improvement in mechanical properties at extremely low loading of MWCNTs greatly exceeds previous reports of semicrystalline polymers reinforced with CNTs, which may be broadly attributed to the successful dispersion and compatibilization of disentangled MWCNTs into the semicrystalline PP matrix. Our novel pretreatment method offers exciting opportunities to significantly improve material properties, particularly electrical conductivity, dimensional stability, thermal stability, and heat deflection temperature, without sacrificing processability or environmental stability. The present discussion will focus on identifying the potential mechanisms responsible for the greatly improved modulus observed in this work and to consider the generality and broader applications of our findings.

It is well-known that the presence of CNTs dramatically modifies the morphology of semicrystalline polymers. In this work, DSC and WAXD measurements confirmed that the degree of crystallinity is not affected by the MWCNTs, and no changes in lamellar orientation or anisotropy were detected with SAXS and OM observations. The nucleating ability of the MWCNTs substantially reduces spherulite diameter and completely suppresses the formation of β-form crystal at loading of only 0.1 wt % F-MWCNT. Given the relatively small

Table 3. Summary of Tensile Properties of PP/F-MWCNT Composites Prepared by Injection-Molding and Compression-Molding

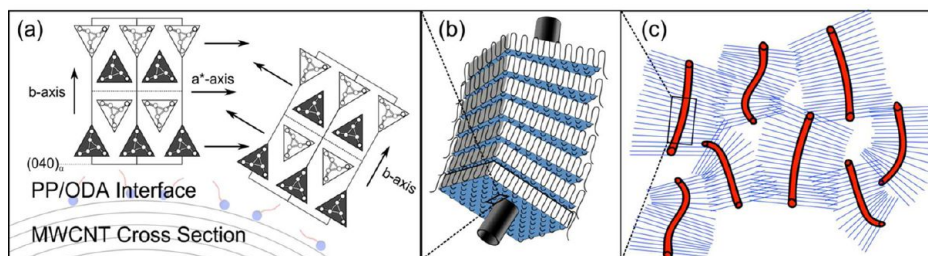|	injection-molded			compression-molded		
	E (GPa)	σ_y (MPa)	ε_B (%)	E (GPa)	σ_y (MPa)	ε_B (%)
neat PP	1.5 ± 0.04	34.3 ± 0.82	>300	1.7 ± 0.05	34.0 ± 2.3	9 ± 1
0.1 wt % F-MWCNT	2.1 ± 0.05	39.8 ± 1.70	10 ± 4	2.0 ± 0.09	33.4 ± 0.9	5 ± 1
0.6 wt % F-MWCNT	2.2 ± 0.20	40.7 ± 1.50	12 ± 8			
0.1 wt % P-MWCNT	1.6 ± 0.06	34.3 ± 0.61	>300	1.7 ± 0.17	33.0 ± 1.4	8 ± 3
0.5 wt % ODA	1.4 ± 0.10	37.7 ± 0.70				

Figure 9. Schematic showing structure of PP/F-MWCNT across multiple length scales. (a) Proposed orientation of the PP unit cell at the F-MWCNT surface, where (040) plane of α-form crystal unit cell is parallel and the b-axis is perpendicular to the long axis of the MWCNT. The c-axis of the unit cell is projected out of the page. Each layer corresponds to a population of chiral helices, represented by triangles, with antichiral alternating layers. The ODA functional group is shown schematically as a primary head and long tail corresponding to the covalent amide linkage ((C=O)NH) and long-chain alkyl tail ($C_{18}H_{37}$), respectively. (b) Bulk structure of PP/F-MWCNT with localized transcrystalline domains extended radially from the F-MWCNT surface. (c) Network of individual MWCNTs with interfacially crystallized PP domains extending from surface.

fraction of β-form crystallites in the neat PP, this contribution is not sufficient to account for the magnitude of modulus improvement or the significant decrease in ductility in both PP/F-MWCNT systems. SAXS measurements show the MWCNTs do not change the 2D lamellae structure of the PP, and no significant change in lamellae thickness could be identified. These results show that the indirect contributions of the MWCNTs are not sufficient to adequately describe the change in mechanical behavior observed in the PP/F-MWCNT systems, which indicates that additional, direct reinforcement mechanisms must also be present.

During injection-molding, the molten PP/MWCNT resin is forced into a cold mold cavity and subsequently crystallizes in the presence of a highly heterogeneous distribution of thermal stresses.[63] The PP chains are significantly stretched and uncoiled due to the shear and elongational stresses at the mold entrance but tend to rapidly relax during cooling and are generally unoriented in the core region. The shearing stresses also likely extend the individually dispersed MWCNTs in the flow direction, which increases the available surface area and favors a high nucleation density along the entire MWCNT surface. Because of the mutual orientation of the PP chains and MWCNTs in the flow direction during molding, PP chains at the MWCNT surface will tend to be anchored with molecular axis parallel to the long axis of the MWCNTs. Upon cooling, crystal growth proceeds fastest perpendicular to the MWCNT axis, which results in the highly ordered, transcrystalline PP domains observed in Figures 1 and 2. The WAXD measurements revealed that the (040) lattice planes of the MWCNT-nucleated PP crystals are preferentially oriented in the molding direction and that crystal growth is favored in the respective b-axis direction. A schematic of the proposed mode of crystal nucleation is provided in Figure 9a, where the shaded and white triangles correspond to the two different chiral populations of PP molecules and are shown with c-axis oriented out of the page. The c-axis of the PP unit cell is depicted parallel to the MWCNT axis, which is in agreement with our description of shear-induced alignment during molding and consistent with most previous reports.[64] It is clear from Figure 9a that even though crystal growth along the a^*-axis is preferred,[65] the high density of active crystal nuclei behaves as lateral barriers and force crystal growth along the b-axis.

For the purpose of this discussion, the most significant consequence of the confined mode of crystal growth is the interaction of extended MWCNTs with highly oriented, uniform transcrystalline PP layers, which is illustrated in Figure 9b. The nucleated crystallites are exclusively α-form PP, and the

size and perfection of the crystals are increased relative to the neat PP. Several recent reports have suggested that uniform interfacial crystallization results in excellent load transfer efficiency and high interfacial adhesion between the polymer and CNT.[65] Furthermore, the mismatch in the coefficient of thermal expansion between the PP and CNTs may favor mechanical interlocking between phases due to thermal residual compressive stresses.[66,67] The resulting global microstructure, illustrated in Figure 9c, consists of uniformly dispersed, high aspect ratio F-MWCNTs that are preferentially aligned in the molding direction and integrated within an array of transcrystalline α-form crystals that extend along the length of the MWCNT. The TEM micrographs in Figure 2 support the proposed microstructure, and the TEMT results in Figure 3 provide the first unambiguous evidence that the PP crystal lamellae and F-MWCNTs are spatially associated in an injection-molded nanocomposite. At low loading, the extended domains will overlap and result in significant load transfer between reinforced regions. This mechanism of global reinforcement is similar to our previous findings in epoxies[68,69] but is more effective in this case because the transcrystalline domains effectively multiply the volume fraction of MWCNTs.

The formation of a well-defined transcrystalline interface is not unique to this work and may be a general feature of PP/CNT systems.[22,33,34] The substantial increase in modulus and associated decrease in ductility has not been reported, which we attribute to previous challenges in achieving adequate dispersion of CNTs in large quantities and lack of compatibility between phases. The compatibilization is extremely important in this context because it provides a mechanism for the F-MWCNTs to interact and transfer load between phases. The uniaxial tension and DMA findings indicate that the F-MWCNTs are able to directly reinforce crystalline domains and amorphous interlamellae layers. In this case, the MWCNTs serve as physical anchors and provide continuity between crystalline lamellae, which suggests that they behave as "super" tie-chain molecules. The anchoring of crystalline lamellae will also likely prevent significant intralamellar slip and other dislocation processes in the crystal phase, which should severely inhibit plastic deformation upon yielding.

The above description is consistent with the uniaxial tension results of the PP/F-MWCNT (0.1 wt %) system, which show limited interlamellar deformation and molecular orientation prior to fracture. At slightly higher loading of 0.6 wt % F-MWCNT, there is no evidence of plasticity or yield behavior during uniaxial tension. From the SAXS and DMA results, we proposed that the higher loading of F-MWCNTs are not well-

integrated in the transcrystalline structure and therefore introduce more significant disorder between ordered domains. The observed brittle fracture prior to necking indicates that the resulting microstructure from the higher loading of F-MWCNTs completely inhibits intralamellar deformation. The relatively high elongation at break of the PP/P-MWCNT (0.1 wt %) system is attributed to the poor integration of the noncompatibilized CNTs within the lamellar structure of the matrix. Further work is being pursued to more explicitly identify the deformation and fracture mechanisms of these systems.

The proposed reinforcement mechanism does not depend on any particular features of our nanoplatelet-dispersion method and requires only excellent dispersion and good compatibility between polymer and CNT. This description should therefore be general to any PP/MWCNT systems. The unique feature of the method used in this work is that the MWCNTs are disentangled and isolated prior to dispersing in the PP matrix. Therefore, no significant mechanical forces are required during processing. This approach preserves the useful properties of the MWCNTs, and the stability of the dispersion depends only on the thermal stability and compatibility of the functional group. Furthermore, there is no need to modify the properties of the neat PP matrix through grafting reactions or to introduce surfactants or interfacial agents that may diminish performance and environmental stability. This should enable the production of PP/F-MWCNT nanocomposites using standard processing methods and equipment and is therefore suitable for high volume production. As the interaction between the PP matrix and the F-MWCNTs is governed by the selection of functional group, this approach may be easily adapted to other semicrystalline polymers provided that sufficient compatibility is achieved.

5. CONCLUSIONS

Disentangled MWCNTs were functionalized with ODA and uniformly dispersed in a commercial grade PP by injection-molding. The mechanical properties of the PP were substantially enhanced at low loading but provided relatively little additional improvement at higher loading. The dispersion approach used in this work reduced the critical concentration for bulk modification of the PP crystal structure and resulted in preferential crystal growth due to the orientation and extension of the MWCNTs during injection molding. The F-MWCNTs partially influence the tensile properties by modifying the crystal phase of the PP and are proposed to additionally reinforce multiple lamellar domains and amorphous regions between crystallites as "super"-tie chains. The process may be used in high-volume commercial processing approaches and can be modified by appropriate selection of functionality for use in any polymer matrix.

ASSOCIATED CONTENT

Ⓢ Supporting Information

TEMT video of PP/F-MWCNT (0.1 wt %); optical micrograph showing spherulitic crystal structure of PP/ODA (0.5 wt %); WAXD patterns of compression-molded PP composite systems; 2D-SAXS profiles of PP composite systems; 1D correlation function from SAXS; DMA of injection-molded PP composite systems. This material is available free of charge via the Internet at http://pubs.acs.org.

AUTHOR INFORMATION

Corresponding Author

*Fax +1 979 845-3081; e-mail address:hjsue@tamu.edu.

Author Contributions

The manuscript was written through contributions of all authors. All authors have given approval to the final version of the manuscript.

Author Contributions

‖These authors contributed equally.

Notes

The authors declare no competing financial interest.

ACKNOWLEDGMENTS

REFERENCES

(1) Cadek, M.; Coleman, J. N.; Ryan, K. P.; Nicolosi, V.; Bister, G.; Fonseca, A.; Nagy, J. B.; Szostak, K.; Beguin, F.; Blau, W. J. *Nano Lett.* **2004**, *4*, 353−356.

(2) Yang, B. X.; Shi, J. H.; Pramoda, K.; Goh, S. H. *Compos. Sci. Technol.* **2008**, *68*, 2490−2497.

(3) Pujari, S.; Ramanathan, T.; Kasimatis, K.; Masuda, J.; Andrews, R.; Torkelson, J. M.; Brinson, L. C.; Burghardt, W. R. *J. Polym. Sci., Polym. Phys.* **2009**, *47*, 1426−1436.

(4) Simmons, J. G. *J. Appl. Phys.* **1963**, *34*, 1793−1803.

(5) Jeon, K.; Lumata, L.; Tokumoto, T.; Steven, E.; Brooks, J.; Alamo, R. G. *Polymer* **2007**, *48*, 4751−4764.

(6) Jeon, K.; Warnock, S.; Ruiz Orta, C.; Kismarahardja, A.; Brooks, J.; Alamo, R. G. *J. Polym. Sci., Part B: Polym. Phys.* **2010**, *48*, 2084−2096.

(7) Girifalco, L. A.; Hodak, M.; Lee, R. S. *Phys. Rev. B* **2000**, *62*, 13104.

(8) Qin, Y.; Liu, L.; Shi, J.; Wu, W.; Zhang, J.; Guo, Z. X.; Li, Y.; Zhu, D. *Chem. Mater.* **2003**, *15*, 3256−3260.

(9) Grady, B. P.; Pompeo, F.; Shambaugh, R. L.; Resasco, D. E. *J. Phys. Chem. B* **2002**, *106*, 5852−5858.

(10) Causin, V.; Yang, B. X.; Marega, C.; Goh, S. H.; Marigo, A. *Eur. Polym. J.* **2009**, *45*, 2155−2163.

(11) Valentini, L.; Biagiotti, J.; Kenny, J. M.; Santucci, S. *J. Appl. Polym. Sci.* **2003**, *87*, 708−713.

(12) Bikiaris, D.; Vassiliou, A.; Chrissafis, K.; Paraskevopoulos, K. M.; Jannakoudakis, A.; Docoslis, A. *Polym. Degrad. Stabil.* **2008**, *93*, 952−967.

(13) Kashiwagi, T.; Grulke, E.; Hilding, J.; Harris, R.; Awad, W.; Douglas, J. *Macromol. Mater. Eng.* **2002**, *23*, 761−765.

(14) Kashiwagi, T.; Grulke, E.; Hilding, J.; Groth, K.; Harris, R.; Butler, K.; Shields, J.; Kharchenko, S.; Douglas, J. *Polymer* **2004**, *45*, 4227−4239.

(15) Yang, J.; Lin, Y.; Wang, J.; Lai, M.; Li, J.; Liu, J.; Tong, X.; Cheng, H. *J. Appl. Polym. Sci.* **2005**, *98*, 1087−1091.

(16) Kharchenko, S. B.; Douglas, J. F.; Obrzut, J.; Grulke, E. A.; Migler, K. B. *Nat. Mater.* **2004**, *3*, 564−568.

(17) Kashiwagi, T.; Du, F.; Douglas, J. F.; Winey, K. I.; Harris, R. H.; Shields, J. R. *Nat. Mater.* **2005**, *4*, 928−933.

(18) Chu, C.-C.; White, K. L.; Liu, P.; Zhang, X.; Ryousho, Y.; Sue, H. J. *Carbon* **2012**, *50*, 4711−4721.

(19) Bhattacharyya, A. R.; Sreekumar, T. V.; Liu, T.; Kumar, S.; Ericson, L. M.; Hauge, R. H.; Smalley, R. E. *Polymer* **2003**, *44*, 2373−2377.

(20) Assouline, E.; Lustiger, A.; Barber, A. H.; Cooper, C. A.; Klein, E.; Wachtel, E.; Wagner, H. D. *J. Polym. Sci., Polym. Phys.* **2003**, *41*, 520−527.

(21) Manchado, M. A.; Valentini, L.; Biagiotti, J.; Kenny, J. M. *Carbon* **2005**, *43*, 1499−1505.

(22) Miltner, H. E.; Grossiord, N.; Lu, K.; Loos, J.; Koning, C. E.; Van Mele, B. *Macromolecules* **2008**, *41*, 5753−5762.

(23) Razavi-Nouri, M. *J. Appl. Polym. Sci.* **2012**, *124*, 2541−2549.

(24) Sun, D.; Everett, W. N.; Chu, C. C.; Sue, H. J. *Small* **2009**, *5*, 2692−2697.

(25) White, K. L.; Shuai, M.; Zhang, X.; Sue, H. J.; Nishimura, R. *Carbon* **2011**, *49*, 5124−5131.

(26) Zhang, X.; Sue, H. J.; Nishimura, R. *J. Mater. Chem.* **2012**, *22*, 6156−6164.

(27) Sun, L.; Boo, W. J.; Sue, H. J.; Clearfield, A. *New J. Chem.* **2006**, *31*, 39−43.

(28) Sun, L.; Boo, W. J.; Browning, R. L.; Sue, H. J.; Clearfield, A. *Chem. Mater.* **2005**, *17*, 5606−5609.

(29) Boo, W. J.; Sun, L. Y.; Liu, J.; Clearfield, A.; Sue, H. J.; Mullins, M. J.; Pham, H. *Compos. Sci. Technol.* **2007**, *67*, 262−269.

(30) Frank, J. *Electron Tomography: Three-Dimensional Imaging with the Transmission Electron Microscope*; Plenum: New York, 1992.

(31) Jinnai, H.; Spontak, R. J.; Nishi, T. *Macromolecules* **2010**, *43*, 1675−1688.

(32) Park, J.; Eom, K.; Kwon, O.; Woo, S. *Microsc. Microanal.* **2001**, *7*, 276−286.

(33) Zhang, S.; Minus, M. L.; Zhu, L.; Wong, C. P.; Kumar, S. *Polymer* **2008**, *49*, 1356−1364.

(34) Lu, K.; Grossiord, N.; Koning, C. E.; Miltner, H. E.; Mele, B.; Loos, J. *Macromolecules* **2008**, *41*, 8081−8085.

(35) Jinnai, H.; Spontak, R. J. *Polymer* **2009**, *50*, 1067−1087.

(36) Jinnai, H.; Sawa, K.; Nishi, T. *Macromolecules* **2006**, *39*, 5815−5819.

(37) Jinnai, H.; Nishikawa, Y.; Spontak, R. J.; Smith, S. D.; Agard, D. A.; Hashimoto, T. *Phys. Rev. Lett.* **2000**, *84*, 518−521.

(38) Jinnai, H.; Kaneko, T.; Matsunaga, K.; Abetz, C.; Abetz, V. *Soft Matter* **2009**, *5*, 2042−2046.

(39) Jinnai, H.; Spontak, R. J.; Nishi, T. *Macromolecules* **2010**, *43*, 1675−1688.

(40) Zeng, Q.; Yu, A.; Lu, G. *Prog. Polym. Sci.* **2008**, *33*, 191−269.

(41) Nishioka, H.; Niihara, K. I.; Kaneko, T.; Yamanaka, J.; Inoue, T.; Nishi, T.; Jinnai, H. *Compos. Interfaces* **2006**, *13*, 589−603.

(42) Jinnai, H.; Shinbori, Y.; Kitaoka, T.; Akutagawa, K.; Mashita, N.; Nishi, T. *Macromolecules* **2007**, *40*, 6758−6764.

(43) Turner-Jones, A.; Aizlewood, J. M.; Beckett, D. R. *Makromol. Chem.* **1964**, *75*, 134−158.

(44) Iijima, M.; Strobl, G. *Macromolecules* **2000**, *33*, 5204−5214.

(45) Padden, F. J.; Keith, H. D. *J. Appl. Phys.* **1966**, *37*, 4013−4020.

(46) Lovinger, A. J. *J. Polym. Sci., Part B: Polym. Phys.* **1983**, *21*, 97−110.

(47) Varga, J. *J. Macromol. Sci., Part B* **2002**, *41*, 1121−1171.

(48) Natta, G.; Corradini, P. *Nuovo. Cimento. Suppl.* **1960**, *15*, 40.

(49) Inada, T.; Masunaga, H.; Kawasaki, S.; Yamada, M.; Kobori, K.; Sakurai, K. *Chem. Lett.* **2005**, *34*, 524−525.

(50) Jacoby, P.; Bersted, B. H.; Kissel, W. J.; Smith, C. E. *J. Polym. Sci., Polym. Phys.* **1986**, *24*, 461−491.

(51) Fujiyama, M.; Wakino, T. *J. Appl. Polym. Sci.* **1991**, *42*, 9−20.

(52) Zheng, Q.; Shangguan, Y.; Yan, S.; Song, Y.; Peng, M.; Zhang, Q. *Polymer* **2005**, *46*, 3163−3174.

(53) Jin, Y.; Rogunova, M.; Hiltner, A.; Baer, E.; Nowacki, R.; Galeski, A.; Piorkowska, E. *J. Polym. Sci., Part B: Polym. Phys.* **2004**, *42*, 3380−3396.

(54) Avila-Orta, C. A.; Medellin-Rodriguez, F. J.; Davila-Rodriguez, M. V.; Aguirre-Figueroa, Y. A.; Yoon, K.; Hsiao, B. S. *J. Appl. Polym. Sci.* **2007**, *106*, 2640−2647.

(55) Chu, B.; Hsiao, B. S. *Chem. Rev.* **2001**, *101*, 1727−1762.

(56) Xia, Z.; Sue, H. J.; Wang, Z.; Avila-Orta, C. A.; Hsiao, B. S. *J. Macromol. Sci., Part B: Phys.* **2001**, *40*, 625−638.

(57) Strobl, G. R.; Schneider, M. *J. Polym. Sci., Part B: Polym. Phys.* **1980**, *18*, 1343−1359.

(58) McCrum, N. G. *Polymer* **1984**, *25*, 299.

(59) Crissman, J. M.; Sauer, J. A.; Woodward, A. E. *J. Polym. Sci., Polym. Chem.* **1964**, *2*, 5075−5091.

(60) Byrne, M. T.; Gun'ko, Y. K. *Adv. Mater.* **2011**, *22*, 1672−1688.

(61) Personal communication with Arkema to H.J.S., 2012.

(62) Rabb, M.; Scudla, J.; Kolarik, J. *Eur. Polym. J.* **2004**, *40*, 1317−1323.

(63) Fujiyama, M.; Wakino, T. *J. Appl. Polym. Sci.* **1991**, *43*, 97−128.

(64) Ning, N.; Fu, S.; Zhang, W.; Chen, F.; Wang, K.; Deng, H.; Zhang, Q.; Fu, Q. *Prog. Polym. Sci.* **2011**, *37*, 1425−1455.

(65) Clark, E. J.; Hoffman, J. D. *Macromolecules* **1984**, *17*, 878−885.

(66) Liao, K.; Li, S. *Appl. Phys. Lett.* **2001**, *79*, 4225−4227.

(67) Wong, M.; Paramsothy, M.; Xu, X. J.; Ren, Y.; Li, S.; Liao, K. *Polymer* **2003**, *44*, 7757−7764.

(68) White, K. L.; Sue, H. J. *Polym. Eng. Sci.* **2011**, *51*, 2245−2253.

(69) White, K. L.; Sue, H. J. *Polymer* **2012**, *53*, 37−42.